

3D reconstruction of compressible flow by synchronized multi-camera BOS

F. Nicolas, D. Donjat, F. Micheli, O. Léon, F. Champagnat, G. Le Besnerais

Received: date / Accepted: date

Abstract An original one-step 3DBOS method for reconstruction of instantaneous 3D density fields from a limited number of Background Oriented Schlieren (BOS) images has recently been proposed by [Nicolas et al \(2016\)](#). The present paper investigates the application of this method to the case of compressible flows such as underexpanded jets. First, an optimization of a 2D BOS setup is conducted in order to mitigate the intense local blurs observed in raw BOS images and caused by strong density gradients present in the jets. It is demonstrated that a careful choice of experimental conditions enables one to obtain sharp deviation fields from 2D BOS images. Second, a 3DBOS experimental bench involving 12 synchronized cameras is specifically designed for the present study. It is shown that the 3DBOS method is able to provide physically consistent 3D reconstructions of instantaneous and mean density fields for various underexpanded jet flows issued into quiescent air. Finally, relying on results obtained for a moderately underexpanded jet, an analysis of the jet density structure is conducted through phase-averaging based on a Proper Orthogonal Decomposition (POD), highlighting the development of a dominant Kelvin-Helmholtz instability.

Keywords BOS · Tomography · Underexpanded Jet

F. Nicolas, D. Donjat, F. Micheli, O. Léon
 ONERA, DMAE, 2 Avenue Edouard Belin, 31400 Toulouse, FRANCE
 Tel.: +335 62 25 28 08
 Fax: +123-45-678910
 E-mail: francois.nicolas@onera.fr (corresponding author)

G. Le Besnerais, F. Champagnat
 ONERA, DTIM, Chemin de la Hunière, 91123 Palaiseau, FRANCE

1 Introduction

1.1 Underexpanded jets

Underexpanded jets have been studied for a long time. The main application are obviously jet engines but also the study of pressurized tank leakages. In the case of jet engine, we encountered the underexpanded jet configuration when the nozzle exit is not adapted, that is to say that the high pressure gas has not expanded enough to reach the ambient pressure. On the contrary, we speak of overexpanded jet when the exit pressure is lower than the ambient one. Being not adapted, the jet thrust is not optimal and additional noise is generated referred as shock-associated noise. Moreover, a complex flow topology is formed. Numerous studies has focused on the comprehension underexpanded jet flows and on specific mechanism being the source of instabilities such as the production of screech noise which is feedback loop between Kelvin-Helmholtz or hydrodynamic instabilities ([Powell 1953](#)). Underexpanded jets are characterized by the Nozzle Pressure Ratio (NPR), which is equal to the ratio between the total pressure (P_0) and the ambient one (P_a). Some studies, also referred to the fully expanded jet Mach number defined as

$$M_j = \sqrt{\frac{2}{\gamma-1} (NPR^{\frac{\gamma-1}{\gamma}} - 1)}. \quad (1)$$

It corresponds to the exit Mach number providing an adapted jet. Without a divergent nozzle the jet can't expand and it is necessarily underexpanded. Then it shows a typical succession of expansion fans and reflected shock waves also referred as the diamond shock cells. As the NPR increases, the spacing length of shock-cells increase and at some point the flow topology changes. A schematic view of a highly underexpanded jet is presented in figure 1.

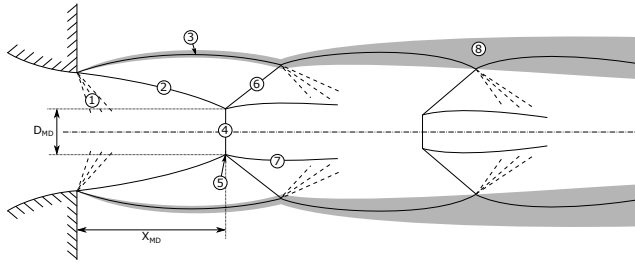


Fig. 1: Schematic view of the flow topology for a highly underexpanded jet (NPR = 4-7). 1-Expansion fan. 2-Barrel shock. 3-Mixing layer iso-bar line. 4- Mach disk. 5- Triple point. 6-Reflected oblique shock. 7-slip line. 8-Mixing layer.

From the nozzle exit the jet suddenly expand ① in the region delimited by barrel shock ②. Then, the emergence of a Mach disk(MD) ④ is characteristic of highly underexpanded jets. A triple point ⑤ is present at the intersection of the Mach disk , the barrel shock and the reflected shock ⑥ on the isobar line ③ of the mixing layer. The region behind the Mach disk which is a normal shock is subsonic contrary to the region behind the oblique reflected shock. A slip line ⑦ make the distinction between those two regions. Classical parameters of this kind of flows is the MD diameter: D_{MD} and the distance of the MD to the nozzle exit: X_{MD} .

1.2 Measurement techniques

Performing measurement in supersonic jets is quite a challenge for multiple reasons: first, the use of probes (pressure probes, hot wire, ...) is really tricky due to the strong perturbation (shock waves, additional noise) cause by the presence of the probe inside the flow. People focus their attention to non-intrusive techniques such as Laser Doppler Velocimetry (LDV) and Particle Image Velocimetry (PIV). Setting those velocimetry techniques is not simple as well: both rely on particle displacement and a special care need to be done in the choice of tracers allowing a particle-laden flow. However recent study demonstrate the ability of performing such measurement with both LDV ([Feng and McGuirk 2016](#)) and tomo-PIV ([Wernet 2016](#)). [Panda and Seasholtz \(1999\)](#) and [Panda and Seasholtz \(2002\)](#) used a Rayleigh-scattering technique to measure density in underexpanded jets. He shows all the potential of the technique for measuring density fluctuations and density spectra, and gives a better understanding in the screech noise mechanisms by doing correlation with far-field noise measurement ([Panda and Seasholtz 2002](#)). Contrary to LDV and PIV the Rayleigh-scattering technique does not require particles, preventing from disturbing the flow. It rely on the molecules light re-emission. By focusing a laser beam in a small volume (typically about 1 mm side) and using a photon counter, one is

able to measure density. The main uncertainty associated with Rayleigh-scattering measurement is due to the electronic shot noise. The technique is also sensitive to dust particles present in the flow, condensation and the parasite contribution of ambient light.

For a long time supersonic flows have been studied experimentally using refractive index-based optical techniques such as schlieren or shadowgraphy. Those Line-of-Sight(LOS) techniques convert the optical index gradient (schlieren) or the second derivative of the index (shadowgraphy) into intensity variations providing very nice visualizations of flows topology. However, the use of those techniques to obtain quantitative measurements is quite a challenge because of the difficulty to calibrate the system. Moreover, schlieren can only measure one gradient at a time (horizontal or vertical) depending on the knife edge orientation. [Kolhe and Agrawal \(2009\)](#); [Takano et al \(2016\)](#) used rainbow schlieren to reconstruct density volume after calibrating their filter. However, [Kolhe and Agrawal \(2009\)](#) suffers from to low resolution, due to its micro-scale application, to show a precise analysis of the jet topology. Finally, like schlieren, both studies rely on one density gradients which can leads to an erroneous estimation of the density field.

1.3 Background oriented schlieren

Recently, with the major advances accomplish in PIV, a new technique emerged: Background Oriented Schlieren (BOS). BOS is an optical technique aiming at measuring density gradients. It consists in imaging a textured background by a camera, firstly without flow. Then a second picture is taken with a phase object in between the camera and the background. The light rays deflections caused by refractive index variations lead to virtual displacements of the background pattern on the camera sensor. Those displacements can be computed using image correlation methods, such as PIV software, and the deviation maps can be derived from the geometry of the experiment. From deviation maps recorded on the same flow from various viewpoints, the 3D density field can be reconstructed [Atcheson et al \(2008\)](#); [Leopold et al \(2013\)](#); [Ota et al \(2011\)](#) by numerically inverting the ray equation:

$$\varepsilon = \frac{G}{n_{ext}} \int_{s \in ray} \nabla \rho ds \quad (2)$$

This equation links the deviation ε to the integral along the ray of density gradients via the Gladstone-Dale constant G . Since the first BOS developments ([Richard et al \(2002\)](#); [Meier \(2002\)](#)), the use of BOS to investigate supersonic jets has been pointed out. Clem [Clem et al \(2012\)](#) used 2D BOS to investigate screech tones in supersonic jets by measuring shock-spacing length. This characteristic length is also measured by [van Hinsberg and Rösgen \(2014\)](#) on a microjet,

after performing an Abel inversion. [Venkatakrishnan \(2005\)](#); [Tipnis et al \(2013\)](#) derived the 3D density field from BOS images using Filtered Backprojection (FPB) algorithms. They show consistency with the exit density calculated from isentropic relation ([Venkatakrishnan \(2005\)](#)) and a relative agreement with CFD computation ([Tipnis et al \(2013\)](#)). Nevertheless, the poor resolution of their reconstruction make difficult further analysis.

Recently, we have proposed a novel one-step approach for such 3D reconstruction [Nicolas et al \(2016\)](#). In the line of [Atcheson et al \(2008\)](#), our technique is based on simultaneous acquisitions of the flow by several cameras. In [Nicolas et al \(2016\)](#) good results were obtained with 12 cameras on aerothermal test cases where weak density gradients conditions ensure the validity of the paraxial hypothesis for ray trajectories. Moreover, for such incompressible flows, the 3D temperature field can be derived from the density providing a way to validate the reconstruction from independent temperature measurements [Donjat et al \(2015\)](#). The extension of 3DBOS reconstruction to compressible flows is not straightforward.

1.4 Contributions

In this paper, we experimentally analyze an underexpanded jet by BOS. First, in Sec. 2, we mitigate the interfering blurring effect associated with strong gradients in BOS images, which degrades the accuracy of estimated deviations, by optimizing a 2D BOS setup. In Sec. 3, we build a 3D BOS setup in order to capture underexpanded jets instantaneous and mean fields at various NPR. We also evaluate the ability of the 3DBOS algorithm presented in [Nicolas et al \(2016\)](#) to deal with strong density gradients. Finally, in Sec. 4, a moderately underexpanded jet is further analyzed by achieving a POD analysis on instantaneous displacement. This allows us to perform phase-averaged density reconstruction which highlights the Kelvin-Helmoltz vortex shedding.

2 Optimizing the BOS experimental set-up for high resolution measurements

2.1 Astigmatism effects

Shock waves and more generally strong density gradients induce severe light ray deviations. As a result, the whole set of light rays entering the camera may not focus in one pixel anymore: this property is known as astigmatism. The main consequence of this effect is the presence of some blurring on the image as it can be seen on Fig. 2. The blurring effect is damageable for image correlation methods due to the loss of texture in the background image. This leads to a decrease in the correlation score and, for severely blurred areas, the

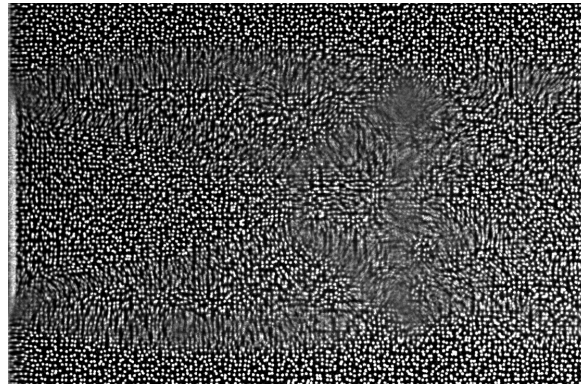


Fig. 2: Example of astigmatism effect induced by an under-expanded shock cell visible on a raw BOS image.

estimation fails. Moreover, such missing deviations, even on restricted parts of the imaged field, can severely degrade the reconstruction of 3D density field. In [Leopold et al \(2013\)](#) a solution based on correlation of color pattern is proposed on a spike and an hemisphere case at Mach 3. They design their color background pre-shifting the red pattern horizontally and vertically, respectively into blue and green patterns. Then, they are able to recover some information on blurred areas by performing the cross-correlation between red and green, and red and blue. This technique could help the correlation for capturing the missing part of the flow. However it is limited to CBOS, it needs to choose correctly the value of the pre-shift and it could be difficult to use for complex instantaneous flows. In the present work, we rely on classical graylevel images but we show that, with a careful choice of experimental conditions, deviation maps with high resolution, comparable to traditional schlieren visualization, can be obtained. In this section, we study the effect of the background position and also the camera aperture both on the sensitivity and reliability of deviation estimation, and on local blur for the study of an underexpanded jet.

2.2 Installation

Our jet facility consisted of a 22 mm diameter convergent nozzle, also referred as a contoured nozzle in the literature, supplied by 80 bar pressurized air tank (see Fig. 3). The air is regulated at a constant temperature equals to 20° C via a 570 kW heater in order to prevent from condensation. The shape of the nozzle ensures a straight sonic condition on the jet exit. Different Nozzle Pressure Ratios are investigated, ranging from 2.1 to 5. For BOS acquisitions, a JAI BM-500GE camera, equipped with a 70 mm lens, is placed at $Z_c = 1\text{ m}$ from the nozzle whereas the background is moved between 18 cm and 2.9 m. For each position ($Z_b = 0.18\text{ m}$, 0.4 m , 1.3 m , 2.9 m), the background is designed in order to get 3-4 pixels dots on the camera image. As our pre-

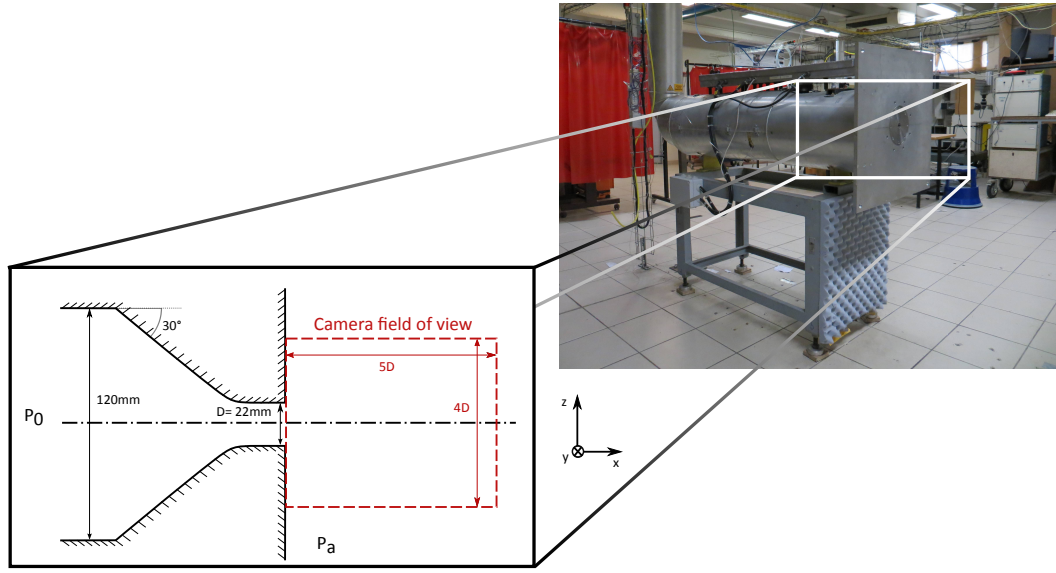


Fig. 3: Jet facility and camera field of view at ONERA Toulouse.

vious studies, we use a semi-random distribution of white dots, that is to say a random distribution into small windows. Illumination is provided by a Quantel Twins BSL double pulsed laser. Both pulses fire during the camera exposure time which leads to a better illumination. The effective exposure time is then equal to the delay between the two laser pulses: 100 ns.

2.3 Parametric analysis

Background oriented schlieren principle is reminded in figure 4. A light ray originated from point P on the background

callly Raffel et al (2000) related to the deviation angle ε via the simplified equation:

$$\Delta x = f \left(\frac{l}{l+m-f} \right) \varepsilon \quad (3)$$

From another hand, the resolution of the measurement is driven by the size of the circle of confusion at the flow location Kirmse et al (2011); Gojani et al (2013); Ota et al (2015). A simplified expression for the circle of confusion is:

$$\delta_t = \frac{f}{l+m} \frac{l}{f} \quad (4)$$

According to Eq. 3 the pixel displacement measured on the camera is proportional to the distance from the background to the flow. Moving the background closer to the experiment reduces both the sensitivity and also the circle of confusion diameter. Among the different background positions we have tested ($l = 2.9\text{ m}$, 1.4 m , 0.4 m and 0.18 m), the smallest position $l = 0.18\text{ m}$ leads to some filtering of the small density gradients such as acoustic waves. The position $l = 0.4\text{ m}$ gives us a minimal sensitivity to correctly captures the different flow features. Then, the aperture parameter can be increased to improve spatial resolution without deteriorating the sensitivity.

For each f-number (7.1, 8, 11, 16 and 22), the laser intensity has been adjusted to get the right amount of light. As the f-number increased, the astigmatism is reduced because the rays suffering from too large deviations do not enter the camera anymore. On Fig. 5, both instantaneous and mean displacement fields are presented. One can see the

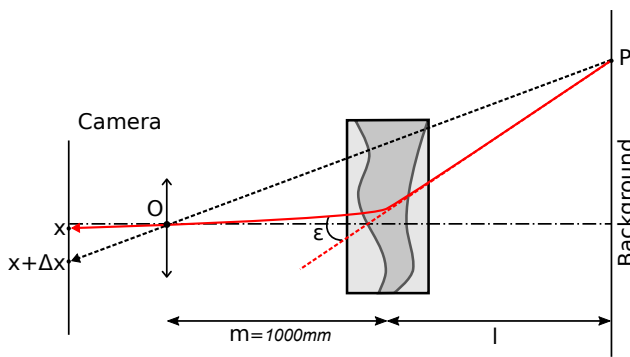


Fig. 4: BOS principle.

strike the CCD in $x + \Delta x$ without any perturbations. In the presence of the flow the ray is deflected and strike the CCD in x . The displacement Δx measured on the CCD is classi-

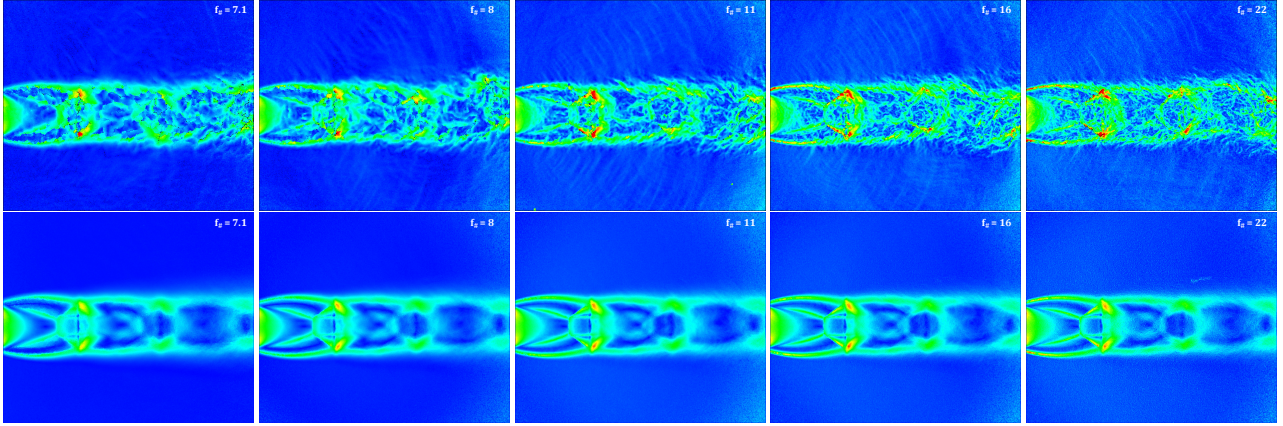


Fig. 5: Influence of the camera aperture on instantaneous BOS field (top) and mean field (bottom). Displacement norm in pixels (scale from 0 to 10).

strong influence of the aperture on instantaneous data: it not only allows a better correlation but reveals finer details on the flow topology which were hidden by the blurring effect. In this case, $f_\# = 16$ represents the best choice with a circle of confusion of 1.25 mm. For larger f-numbers, diffraction impacts the resolution of the background, spreading the dots intensity and increasing correlation noise on BOS images. On the mean displacements fields of Fig. 5, the aper-

(2011). We can also see on Fig. 5 the increase of background noise for $f_\# = 22$ data. This analysis indicate that BOS technique can correctly locates the different flow features, but a relatively large aperture is essential to recover the right levels of displacements and so the right density gradients.

In conclusion of this 2D study, we can say that by choosing wisely its set up, one can acquire very good quality BOS images, with a spatial resolution comparable to traditional schlieren visualization, as demonstrated on Fig. 7.

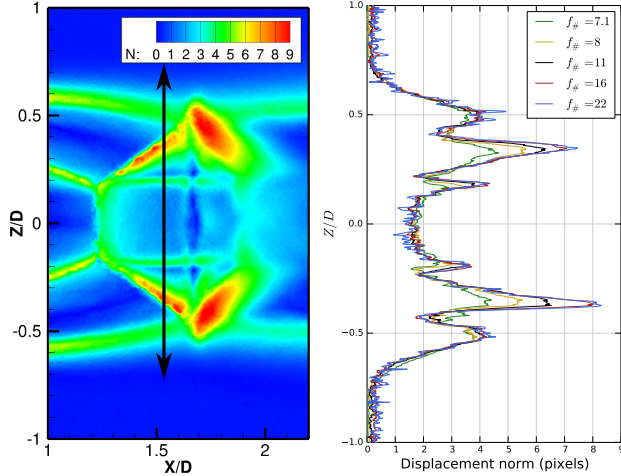


Fig. 6: Displacement norm (N) extracted in $X/D =$ for different f-number.

ture does not seem to have such influence. We take a deeper look on Fig. 6, where slices were extracted at the position $X/D = 1.53$ for all f-number acquisitions. Here it is clear that the spatial filtering of strong gradients associated with the camera aperture is not negligible, especially on the reflected shock wave. For low f-number the image correlation process fails to capture the high density gradient and underestimates the overall displacement as noted by Kirmse et al

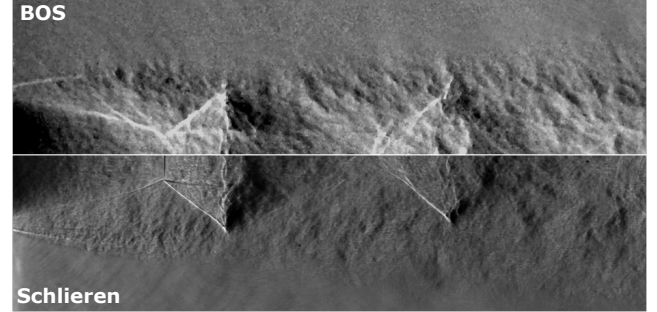


Fig. 7: Comparison between BOS image (top) and schlieren image (bottom). NPR=5.

3 Underexpanded jet 3D density field measurement

3.1 3D BOS bench

Based on the empirical study conducted for 2D BOS in the previous section, we build our 3D BOS experiment bench. Like our previous works, we use 12 cameras. For the study of jets, placing the cameras on half a ring is the configuration chosen by most previous references (Nicolas et al (2016); Atcheson et al (2008); Donnat et al (2015)). We follow this

line by setting up our 12 cameras on a hexagonal bench at a distance $Z_b = 1000$ mm of the jet (Fig. 8). Four background plates covered with 0.2 mm dots are placed at a distance $Z_c = 400$ mm of the jet, facing the cameras. A PIV laser is

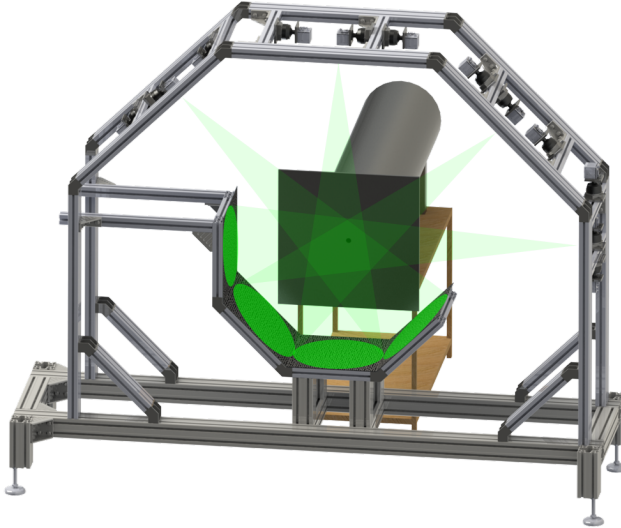


Fig. 8: 3D BOS bench and supersonic hot jet facility.

still used as light source, but we now split the beam into four beams using a separation table made with semi-reflecting mirrors (Fig. 9). Then, the light is driven via liquid guides and spread out onto the backgrounds using 50 mm lenses. This solution enables to cover the 4 background patterns as a

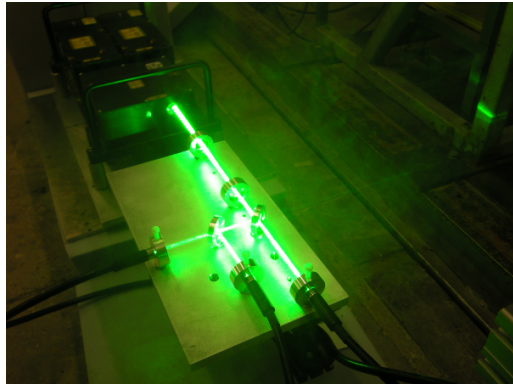


Fig. 9: Laser splitting table, here with 3 beams. In practice, we used 4 beams

whole. Like in the previous 2D case, the two laser pulses are used during the exposure time, both 12 cameras and laser are synchronized with a TTL pulse generator. Unfortunately, the amount of light remaining for each camera does not allow us to use the optimal f-number of 16 and we will operate

the cameras at $f\# = 8$ which leads to a circle of confusion two times bigger (2.5 mm). As we have seen in Sec. 2.3, this choice imply to some filtering of fine scale structures and an underestimation of strong density gradients. At the end, we can also expect some oversmoothing on the final reconstructed density field.

During the acquisition, images are transferred to the RAM memory via an *Enterasys* switch and then moved to SSD disks. This solution enables us to acquire 900 images at 10 Hz. Finally, the multi-cameras system is calibrated as explained in [Le Sant et al \(2014\)](#) by moving a 2D white calibration plate cover with black dots into the common volume of the cameras. For each test condition, $NPR = 2.1, 3, 4$ and 5 (respectively $M_j = 1.09, 1.36, 1.56$ and 1.71), we acquire 900 images by each camera.

3.2 Instantaneous density field reconstruction

The reconstruction process is performed over a volume of $10 \times 7 \times 7$ cm³ using between 40 and 120 million of 0.2 mm side voxels, depending on the flow. A 3D mask is also used to help the reconstruction. As explained in [Nicolas et al \(2016\)](#), the solution to this inverse problem is defined as the minimizer of a compound criterion made of a least square data term penalized with a L2 criterion on density gradients. The optimal regularization parameter λ is chosen accordingly to the L-curve strategy [Hansen \(1992\)](#). Compared to aerothermal cases which were considered in [Nicolas et al \(2016\)](#), the selected parameter is much lower here, (10^{-6} compared to 10^{-4} in [Nicolas et al \(2016\)](#)) preventing from smoothing strong density gradients.

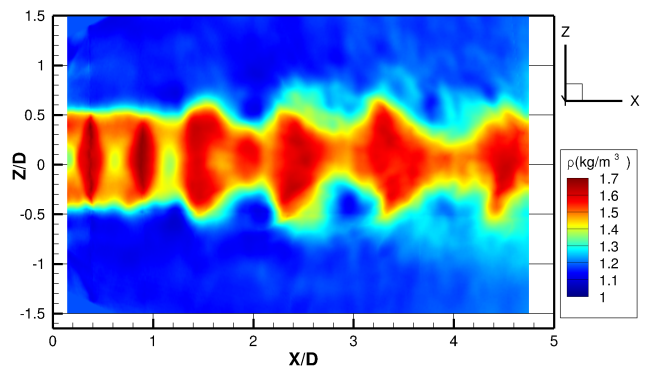


Fig. 10: Instantaneous density field reconstruction for $NPR = 2.1$ case. Slice at $y=0$

First, an instantaneous reconstruction for the moderately underexpanded jet ($NPR=2.1$) has been performed. A slice of the 3D density field is presented in Fig. 10 and iso-surfaces can be seen on Fig. 11. The initial two cells are clearly identifiable. Then the jet topology is much more complex as it is

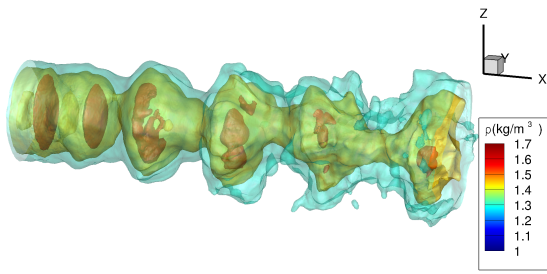


Fig. 11: Instantaneous density field reconstruction for $NPR = 2.1$ case. Iso-density.

destabilized and shock cells aspect is completely distorted. Some over-smoothing on the reconstruction also impacts the quality of the result and the capture of finer scales. Before going deeper in the results, we want to check the performance of our algorithm and verify its ability to deal with strong density gradients. A good way to proceed is to apply our direct operator (raytracer) on the reconstructed density field and compare the resulting deviation maps to the input ones. On Fig. 12, we present on the left part the measured deviations in both horizontal and vertical direction. To the side, corresponding deviation maps, computed with our direct operator, show a good agreement. Those maps are masked to correspond to the 3D mask, that is why outer values are set to zero. Finally, on the right part, slices comparison are provided. Results are very good, even in the sharp region of the first shock cell where discrepancies could have been expected.

3.3 Mean fields analysis

Because the use of a relatively large aperture does not seem to damage the average displacement fields, we push further our algorithm by reconstructing the mean field of different NPRs, from moderately underexpanded jet ($NPR = 2.1$) to highly underexpanded jet ($NPR = 5$). Reconstructions are performed from displacement fields averaged over the 900 images. On Fig. 13, we can see transverse slices and iso-surfaces of the reconstructed density field for each NPR. On the mean field of the moderately underexpanded jet, the train of shock waves is clearly visible in the potential core region. This pattern results from the successive reflection of expansion fans and shock waves on the jet boundary. As the nozzle pressure ratio is increased, the spacing between shock-cells increases. $NPR = 3$ is close to the limit where a change in the flow topology occurs and the Mach disk appears (clearly visible on higher NPR). The result being limited to the intersection volume of all cameras, the very beginning of the jet is not reconstructed. The 3D mask edges visible on slices of Fig. 13 might denote a lack of iterations

in the reconstruction process to allow the regularization to smooth those artifacts.

On left part of Fig. 13, centerlines extraction are plotted. The density ρ is normalized here by ρ_j , the fully expanded density as proposed by Panda [Panda and Seasholtz \(1999\)](#):

$$\rho_j = \frac{P_0}{RT_0} (NPR^{\frac{-1}{\gamma}}) \quad (5)$$

This fully expanded density refers to the density of the jet for perfectly expanded conditions. Because it is not the case, the succession of expansion fans and shock waves oscillates around this value, trying to converge. Note that each plot has been shifted vertically by 1.0. The exit pressure calculated from isentropic relation, for a Mach number equals to one, is also represented on the plot by a dot in $X/D = 0.0$. As the NPR is increased the first expansion is more and more severe. For the $NPR = 5$ case, the Mach disk almost reaches the fully expanded density, and gradually ρ raises above ρ_j with the following shock-cells.

We now focus our attention on the highly underexpanded jet ($NPR = 5$) which is the worst case in terms of density gradient magnitude. We compare our reconstruction with a CFD computation. A DES simulation has been performed with FLUENT 14. The simulation domain is about $25 D$ long and $20 D$ wide. A pipe of $20 D$ is also computed before the nozzle exit. It includes at total of almost 10 Millions of cells. It uses an 2^{nd} order upward scheme in space with an AUSM flux calculation, and a 2^{nd} order implicit scheme in time. We use the Spallart-Allmaras turbulence model for RANS areas. Finally, total pressure and temperature (P_0 and T_0) are imposed at the inlet with a turbulence level of 5 % and atmospheric pressure is set for the outlet boundaries. A comparison is presented on Fig. 14: a transverse slice is presented with the BOS reconstruction on the upper part and the LES simulation on the lower part.

For highly underexpanded jets, a Mach disk (MD) appears. It can be seen on the two shock cells reconstructed. Behind the normal shock of the MD a subsonic zone is present. Then, the flow re-accelerated before encountering a new MD.

The 3D BOS reconstruction shows a very good agreement with the computation. Density levels as well as flow topology are well recovered, especially on the position of the shock-cells. Although the position of the MD seems different for the BOS reconstruction and the CFD on the density slice, the computation of density gradient presented below show a good agreement. Sharpest density gradients located on the Mach disk and on the reflected shock wave are over-smoothed on the reconstruction as expected due to the choice of f -number and not because of the regularization process. Indeed, we checked the choice of our optimal regularization parameter designated by the L-curve by performing another reconstruction with a lower λ : the result being much more noisy shows the same amount of smoothing.

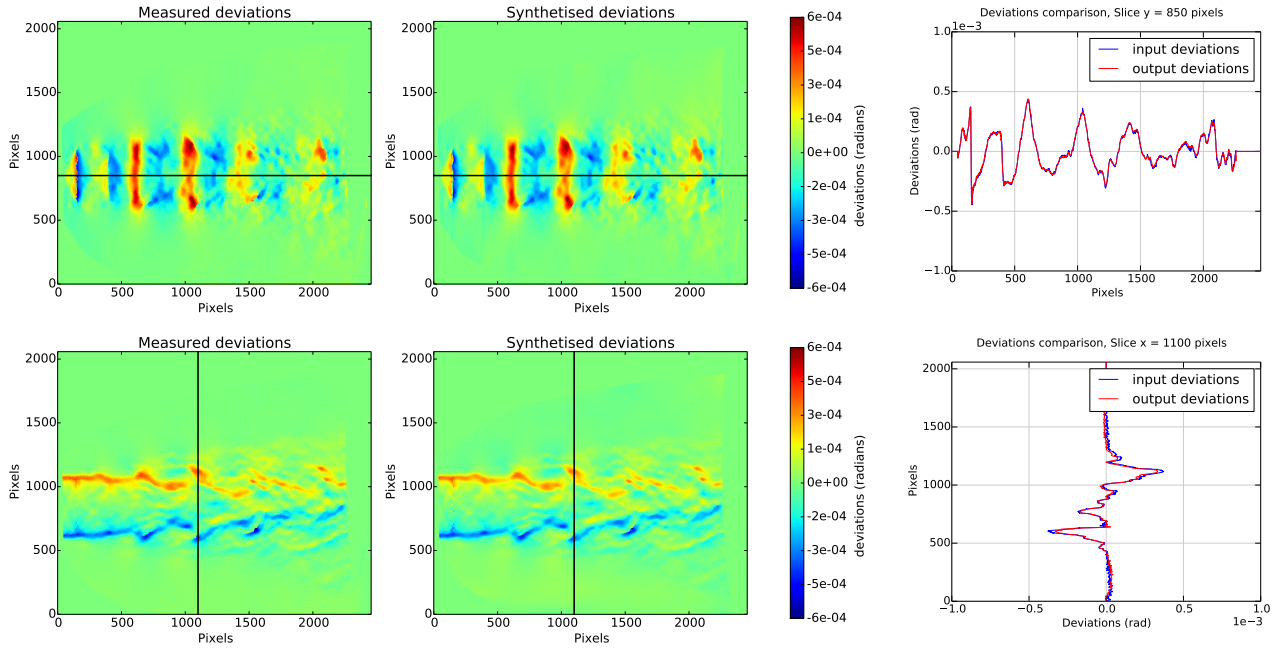


Fig. 12: Deviation map comparisons for x map at the top and z map at the bottom.

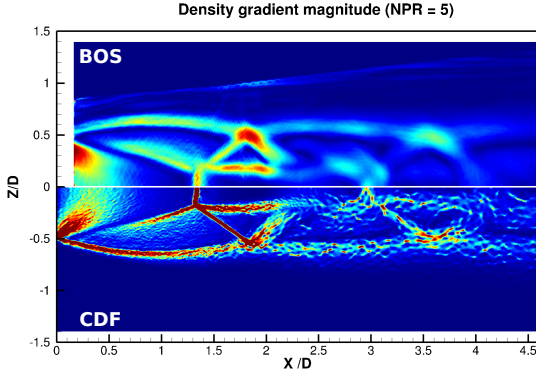
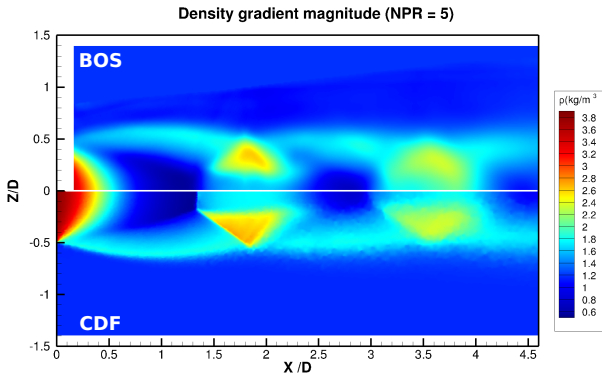


Fig. 14: Mean density field reconstruction for $NPR=5$ case on the left and Density gradient magnitude on the right. Slice at $y = 0$. 3D BOS reconstruction on the upper part and RANS simulation on the lower part.

We also compared in Fig. 11 the position of the MD and his diameter with both schlieren measurements realized previously on the same underexpanded jet and Addy (1981). Although the geometry of the Mach disk is over-smoothed by the reconstruction process, the location and size are quite consistent with this experimental database. Finally, we can also notice that the subsonic region behind the MD is well captured by our technique whereas the Abel inversion and schlieren CT of Takano Takano et al (2016) show some difficulties in this particular region. Moreover, our reconstruction highlights the ring shape of the reflected shock.

4 Vortex shedding analysis

In this section, particular attention is given to the moderately underexpanded jet ($NPR = 2.1$). Indeed, for this case astigmatism perturbations are not too damageable to BOS measurement. Therefore, we finer analyze instantaneous measurement. As we have seen previously, the first two shock cells are very stable contrary to the downstream part of the jet. As described by Panda Powell (1953); Panda (1999), at this operating NPR, two flow structures coexist: the classical train of shock-cells and periodic vortex shedding due to Kelvin-Helmoltz instabilities (K-H). The coupling of this instability and noise production is responsible for screech Panda (1999). Here, the NPR is too low to encounter screech tones, but K-H axisymmetric vortex are still present in the flow. To highlight this phenomenon, we sorted instantaneous displacement maps based on a POD analysis of them. Because our

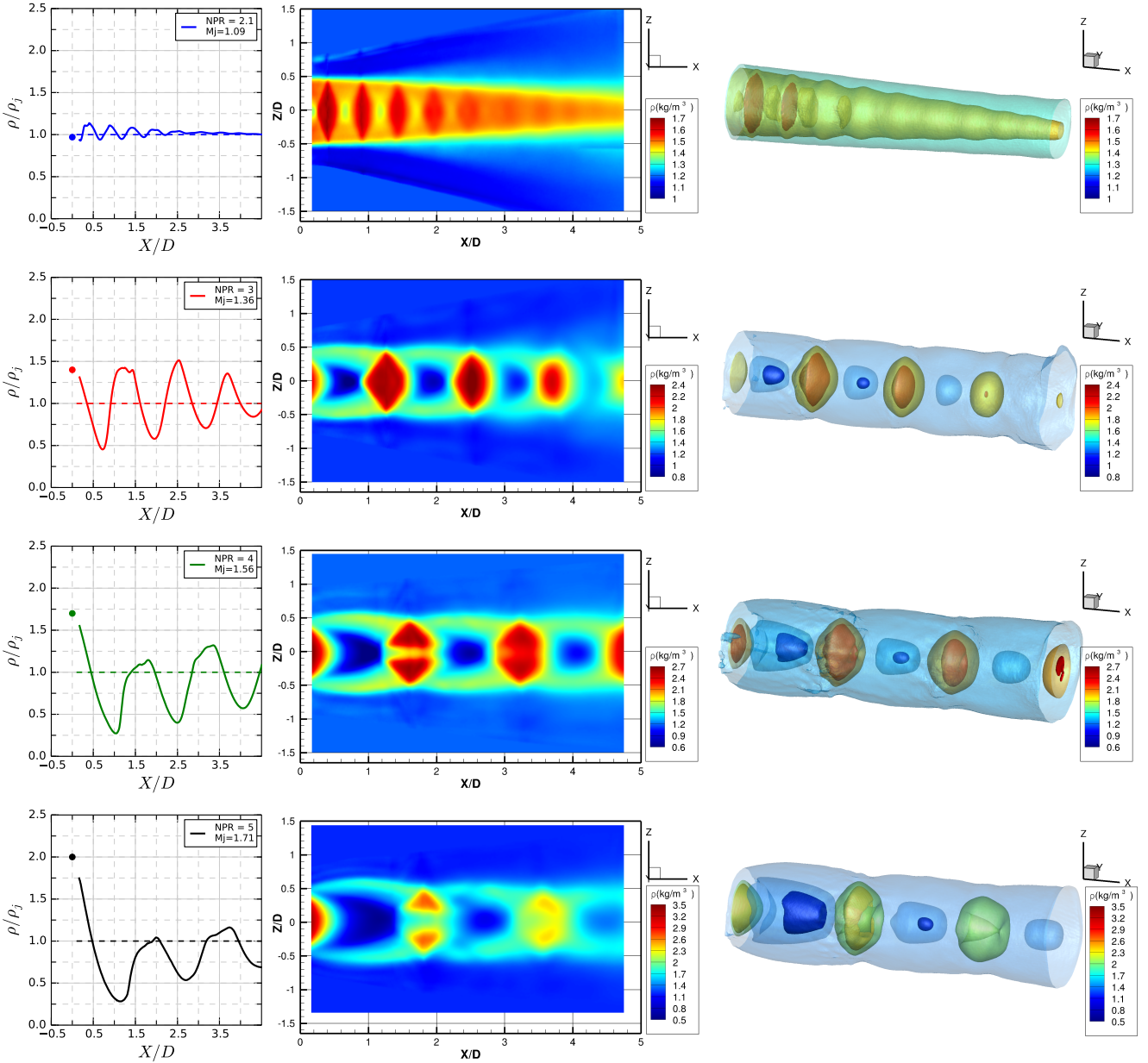


Fig. 13: 3D mean density field reconstruction (transverse slice and iso-surfaces) on the *right* and extracted centerline profiles for each NPR on the *left*.

900 images were acquired at low frequency (10 Hz), this is a way to performed a pseudo-phase averaging. We follow the classical snapshot POD first suggested by Sirovich (1987) and express the POD modes as linear combinations of the $N_t = 900$ snapshots.

First we build a global snapshot matrix U as :

$$\underline{\underline{U}} = \begin{bmatrix} \underline{a}_1 \\ \underline{a}_2 \\ \vdots \\ \underline{a}_{N_t} \end{bmatrix} \quad (6)$$

where \underline{a}_i is defined as:

$$\underline{a}_i = [u_{11}^{(i)}, u_{12}^{(i)}, \dots, u_{nm}^{(i)}, v_{11}^{(i)}, v_{12}^{(i)}, \dots, v_{nm}^{(i)}] \quad (7)$$

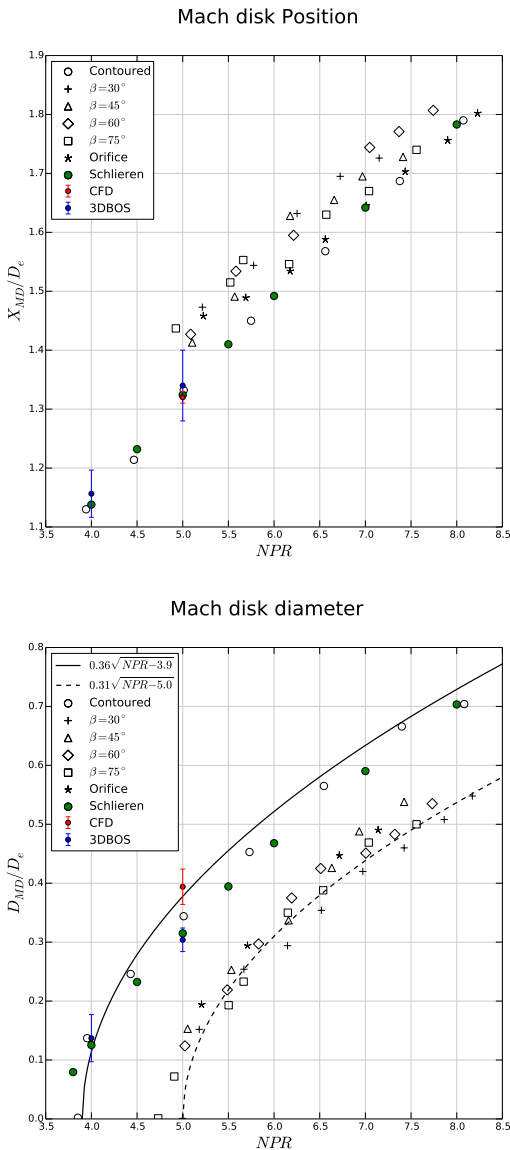


Fig. 15: Evolution of the Mach disk position and diameter with respect to the NPR from [8]. Comparison with the RANS simulation and our schlieren and 3D BOS measurement.

In Eq. 7, $i \in [1, N_t]$, u and v are respectively the horizontal and vertical displacement and, $n * m$ the size of the CCD.

The correlation matrix $\underline{\underline{Q}}$ can be built as :

$$\underline{\underline{Q}} = \frac{1}{N_t} \underline{\underline{U}} \underline{\underline{U}}^T \quad (8)$$

which gives the spatial correlation level between displacement maps.

The POD decomposition of $\underline{\underline{Q}}$ provides spatial eigenfunctions:

$$[\underline{\lambda}, \underline{\psi}] = \text{eig}(\underline{\underline{Q}}) \quad (9)$$

where $\underline{\lambda}$ is the eigenvalues vector allowing POD modes classification and $\underline{\psi}$, the eigenfunctions. Finally, the orthogonal basis of spatial functions $\underline{\phi}$ are obtained from:

$$\underline{\underline{\phi}} = \underline{\underline{U}}^T \underline{\psi} \quad (10)$$

The POD analysis provides a distribution of the normalized eigenvalues shown on Fig. 16. The first two modes concentrate together 50% of the energy, whereas the following are negligible. The resulting spatial functions for POD mode 1 and 2 (Fig. 17) show an identical wave structure with an axial spatial shift revealing a K-H convective instability which grows on the main flow. As the vertical displacements and due to the asymmetry of the jet, one can assume that the fluctuations are mainly confined to the mixing layer.

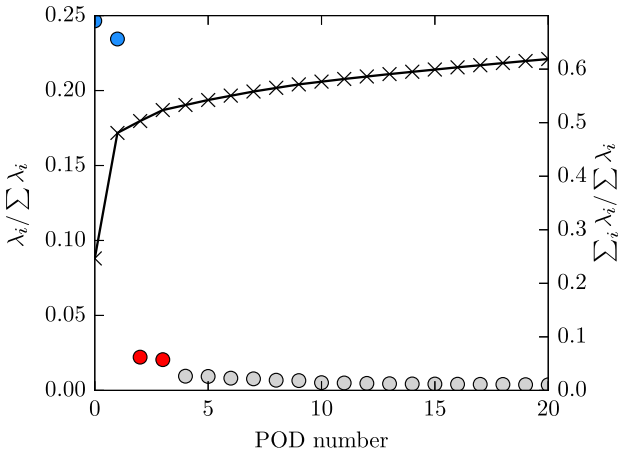


Fig. 16: Normalized eigenvalues in descending order for each POD mode (circle - left axis) - Cumulative evolution of eigenvalues (cross - right axis)

The next step consists in using these modes to build a phase average data defined on the fluctuations observed. We obtain the projection of each snapshot on the $\underline{\phi}$ base following :

$$\underline{\underline{C}} = \underline{\underline{U}} \underline{\phi} \quad (11)$$

Each column i of the matrix $\underline{\underline{C}}$ gives the amplitude of POD modes for each snapshot. The Fig. 19 is a phase portrait of the normalized amplitude of both mode 1 and 2 obtained for the 900 images. The resulting circular-shape cloud of dots is quite uniform, validating the statistical independence of our acquisitions. Finally, we define 15 phase classes and average the corresponding images. The norm of corresponding pseudo-phase averaged displacement map are presented on the left part of Fig. 19. We only present one phase over two. The average position of shock-cells are symbolized with dashed

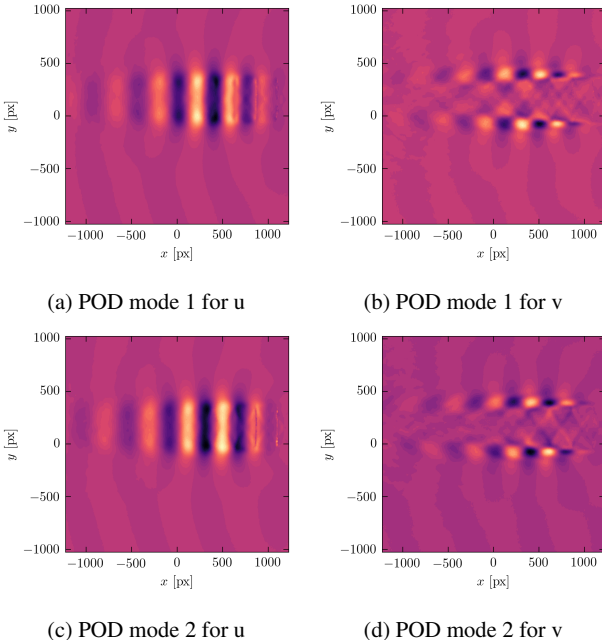


Fig. 17: Spatial functions for POD modes 1 and 2 - u and v displacements

lines and one structure can be followed with the help of the red arrow. From those pseudo-phase averaged displacement map, we performed a 3D reconstruction and the corresponding density field are presented also on Fig. 19: a vertical slice in the middle and iso-surfaces on the right. We well recover the periodic vortex shedding described by Panda, as well on the displacement map as on the density field. The third dimension on density fields bring a new look to the study of such jets. It is clear that the shock-cell pattern is very stable at the beginning, for the first two shock-cell. Although the second one shows a small oscillation, the impact of K-H instabilities are stronger for the following ones: there, the shock-cells are completely distorted by the crossing of the annular vortices. Downstream, from around $X/D = 4$ the turbulence drastically destabilize the jet structure, and the instability is less visible. If, we can feel the presence of those K-H annular vortices on 3D BOS reconstruction, it is quite hard to make them visible on the iso-surfaces images due to their density level which is very close to the ambient density.

5 Conclusion

This paper focuses on 3D density measurement of a compressible jet by BOS. Our contribution is three-fold. First, we have demonstrated that using an optimized set-up and assuming that illumination is sufficient to choose a large aperture number, good quality BOS image can be recorded, leading to estimated deviation of resolution close to schlieren

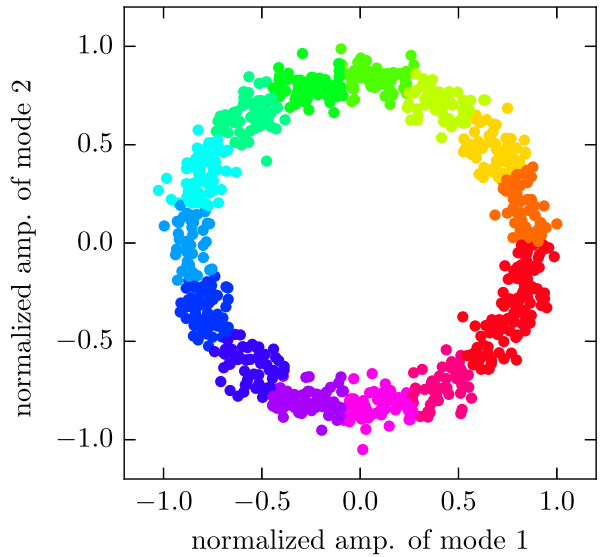


Fig. 18: Phase portrait of the normalized amplitudes for mode 1 and mode 2 given by $(\underline{C}[1,i], \underline{C}[2,i])$ - Colors define our 15 phase classes

techniques. Second, we have built a 3D BOS experiment involving 12 cameras mounted around an underexpanded jet so as to conduct a preliminary evaluation of the 3D BOS methods of [Nicolas et al \(2016\)](#) in compressible conditions. The results are very promising. The estimated flow is slightly oversmoothed, as the result of some filtering involved in the deviation estimation step. We show that astigmatism is responsible for this resulting smoothing and that it can be reduced by working with a high enough f-number. Getting more accurate estimation of deviation is mainly a matter of further improving the experimental set-up, but modification of the correlation method, and in particular use of pixelwise optical flow methods developed in Computer Vision could also bring further gains. Even in the presence of very sharp density gradients, our reconstruction algorithm works well even under the paraxial approximation. Our results show very good agreement as well with the literature as with a CFD computation. Finally, we also demonstrate all the potential of the technique for a better understanding of complex flows at low NPR. Further improvements on the experimental setup and/or on the displacement estimation are still needed to investigate high NPR instantaneous flows. To conclude, measurement of 3D density fields for compressible applications is very challenging. It is also a great interest for comparison with CFD computation and might be a way to better understand light distortion through shock waves. Particle position errors and velocity errors in supersonic PIV could benefit from such measurements and might be corrected with BOS [Elsinga et al \(2005\)](#). Coupled acquisitions

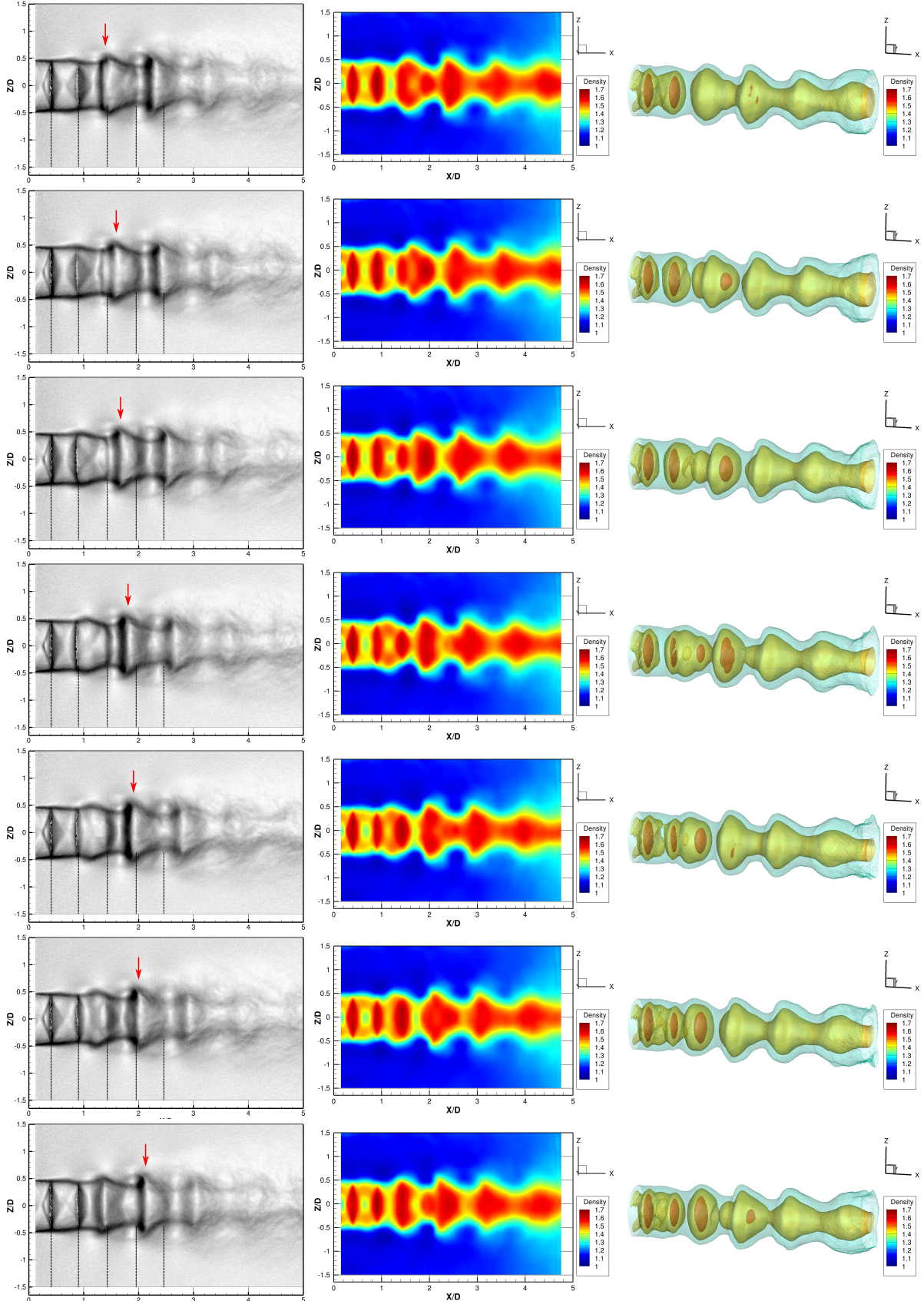


Fig. 19: 7 equi-spaced phase of $NRP = 2$ case. *Left:* raw BOS images of displacement norm (in pixel). *Middle:* Middle Y-slice of the reconstructed 3D density field. *Right:* Iso-surfaces of density.

between 3D BOS and noise measurement could also bring a better understanding of the screech phenomenon.

References

- Addy A (1981) Effects of axisymmetric sonic nozzle geometry on mach disk characteristics. *AIAA Journal* 19(1):121–122
- Atcheson B, Ihrke I, Heidrich W, Tevs A, Bradley D, Magnor M, Seidel HP (2008) Time-resolved 3D capture of non-stationary gas flows. *ACM Transactions on Graphics (Proc SIGGRAPH Asia)* 27(5):132
- Clem MM, Zaman K, Fagan AF (2012) Background oriented schlieren applied to study shock spacing in a screeching circular jet. *AIAA Paper* 403:2012
- Donjat D, Nicolas F, Plyer A, Micheli F, Cornic P, Le Besnerais G, Champagnat F, Le Sant Y, Deluc JM (2015) Study of a co-flowing hot jet: an application of direct 3dbos technique in research wind tunnel
- Elsinga G, van Oudheusden BW, Scarano F (2005) Evaluation of aero-optical distortion effects in piv. *Experiments in fluids* 39(2):246–256
- Feng T, McGuirk JJ (2016) Measurements in the annular shear layer of high subsonic and under-expanded round jets. *Experiments in Fluids* 57(1):1–25
- Gojani AB, Kamishi B, Obayashi S (2013) Review of background oriented schlieren and development for ballistic range applications. In: EPJ Web of Conferences, EDP Sciences, vol 45, p 01034
- Hansen PC (1992) Analysis of discrete ill-posed problems by means of the l-curve. *SIAM review* 34(4):561–580
- van Hinsberg N, Rösger T (2014) Density measurements using near-field background-oriented schlieren. *Experiments in Fluids* 55(4):1–11
- Kirmse T, Agocs J, Schröder A, Martinez Schramm J, Karl S, Hannemann K (2011) Application of particle image velocimetry and the background oriented schlieren technique in the high enthalpy shock tunnel göttingen. *Shock waves* 21:233–241, URL <http://www.springerlink.com/content/u1gu87r818453553/fulltext.pdf>
- Kolhe PS, Agrawal AK (2009) Density measurements in a supersonic microjet using miniature rainbow schlieren deflectometry. *AIAA journal* 47(4):830–838
- Le Sant Y, Todoroff V, Bernard-Brunel A, Le Besnerais G, Micheli F, Donjat D (2014) Multi-camera calibration for 3DBOS. In: 17th Int. Symp. on Applications of Laser Techniques to Fluid Mechanics
- Leopold F, Ota M, Klatt D, Maeno K (2013) Reconstruction of the unsteady supersonic flow around a spike using the colored background oriented schlieren technique. *Journal of Flow Control, Measurement and Visualization* 1(2)
- Meier G (2002) Computerized background-oriented schlieren. *Experiments in Fluids* 33(1):181–187
- Nicolas F, Todoroff V, Plyer A, Le Besnerais G, Donjat D, Micheli F, Champagnat F, Cornic P, Le Sant Y (2016) A direct approach for instantaneous 3D density field reconstruction from background-oriented schlieren (BOS) measurements. *Experiments in Fluids* 57(1):1–21
- Ota M, Hamada K, Kato H, Maeno K (2011) Computed-tomographic density measurement of supersonic flow field by colored-grid background oriented schlieren (cgbos) technique. *Measurement Science and Technology* 22(10):104,011
- Ota M, Leopold F, Noda R, Maeno K (2015) Improvement in spatial resolution of background-oriented schlieren technique by introducing a telecentric optical system and its application to supersonic flow. *Experiments in Fluids* 56(3):1–10
- Panda J (1999) An experimental investigation of screech noise generation. *Journal of Fluid Mechanics* 378:71–96
- Panda J, Seasholtz R (1999) Measurement of shock structure and shock-vortex interaction in underexpanded jets using rayleigh scattering. *Physics of Fluids* (1994–present) 11(12):3761–3777
- Panda J, Seasholtz R (2002) Experimental investigation of density fluctuations in high-speed jets and correlation with generated noise. *Journal of Fluid Mechanics* 450:97–130
- Powell A (1953) On the mechanism of choked jet noise. *Proceedings of the Physical Society Section B* 66(12):1039
- Raffel M, Richard H, Yu Y, Meier G (2000) Background oriented stereoscopic schlieren (boss) for full scale helicopter vortex characterization. In: In 9th international symposium on flow visualization, Heriot-Watt University, Edinburgh, UK
- Richard H, Raffel M, Rein M, Kompenhans J, Meier GEA (2002) Demonstration of the applicability of a Background Oriented Schlieren (BOS) method, Springer Berlin Heidelberg, Berlin, Heidelberg, pp 145–156. DOI 10.1007/978-3-662-08263-8_9, URL http://dx.doi.org/10.1007/978-3-662-08263-8_9
- Sirovich L (1987) Turbulence and the dynamics of coherent structures - parts i-iii. *Quarterly of Applied Mathematics* 45(3):561–590
- Takano H, Kamikihara D, Ono D, Nakao S, Yamamoto H, Miyazato Y (2016) Three-dimensional rainbow schlieren measurements in underexpanded sonic jets from axisymmetric convergent nozzles. *Journal of Thermal Science* 25(1):78–83
- Tipnis T, Finnis M, Knowles K, Bray D (2013) Density measurements for rectangular free jets using background oriented schlieren. *The Aeronautical Journal* 117(1194):771–784
- Venkatakrishnan L (2005) Density measurements in an axisymmetric underexpanded jet by background-oriented schlieren technique. *AIAA journal* 43(7):1574–1579
- Wernet MP (2016) Application of tomo-piv in a large-scale supersonic jet flow facility. *Experiments in Fluids* 57(9):144